



A11106 053035

NIST
PUBLICATIONS

REFERENCE

NISTIR 6749

The Apex Method in Image Sharpening and the Use of Low Exponent Levy Stable Laws

Alfred S. Carasso

U. S. DEPARTMENT OF COMMERCE
Technology Administration
National Institute of Standards
and Technology
Gaithersburg, MD 20899-8230



QC
100
.U56
No. 6749
2001

NIST

**National Institute of Standards
and Technology**
Technology Administration
U.S. Department of Commerce

The Apex Method in Image Sharpening and the Use of Low Exponent Levy Stable Laws

Alfred S. Carasso

U. S. DEPARTMENT OF COMMERCE
Technology Administration
National Institute of Standards
and Technology
Gaithersburg, MD 20899-8230

May 30, 2001



U.S. DEPARTMENT OF COMMERCE
Donald L. Evans, Secretary

NATIONAL INSTITUTE OF STANDARDS
AND TECHNOLOGY
Dr. Karen H. Brown, Acting Director

THE APEX METHOD IN IMAGE SHARPENING AND THE USE OF LOW EXPONENT LÉVY STABLE LAWS

ALFRED S. CARASSO*

Abstract. The APEX method is an FFT-based direct blind deconvolution technique that can process complex high resolution imagery in a few minutes of cpu time on current desktop platforms. The method is predicated on a restricted class of shift-invariant blurs that can be expressed as finite convolution products of two-dimensional radially symmetric Lévy stable probability density functions. This class generalizes Gaussian and Lorentzian densities but excludes defocus and motion blurs. Not all images can be enhanced with the APEX method. However, it is shown that the method can be usefully applied to a wide variety of *real blurred images*, including astronomical, Landsat and aerial images, MRI and PET brain scans, and scanning electron microscope images. APEX processing of these images enhances contrast and sharpens structural detail, leading to very noticeable improvements in visual quality. The discussion includes a documented example of non uniqueness where distinct point spread functions produce high-quality restorations of the same blurred image. Significantly, *low exponent* Lévy point spread functions were detected and used in all the above examples. Such low exponents are exceptional in physical applications where symmetric stable laws appear. In the present case, the physical meaning of these Lévy exponents is uncertain.

Key words. image deblurring; blind deconvolution; direct methods; electronic imaging systems; low exponent stable laws; APEX method; SECB method; non uniqueness; astronomical, Landsat, and SEM images; MRI and PET brain scans.

AMS subject classifications. 35R25, 35B60, 60E07, 68U10.

1. Introduction. The APEX method is an FFT-based direct blind deconvolution technique introduced by the author in [9]. The significance of the present paper lies in the successful use of that method in sharpening a wide variety of *real blurred images*, as opposed to the synthetically blurred images discussed in [9]. The reasons behind these successful applications are not fully understood. Not all images can be usefully enhanced with the APEX method. The present paper is essentially self-contained and may be read independently of [9].

Blind deconvolution seeks to deblur an image without knowing the point spread function (psf) describing the blur. Most approaches to that problem are iterative in nature. Because non uniqueness is compounded with discontinuous dependence on data, such iterative procedures are not always well-behaved. When the iterative process is stable, several thousand iterations may be necessary to achieve useful reconstructions. However, as shown in [9], by limiting the class of blurs, non iterative direct procedures can be devised that accomplish blind deconvolution of 512×512 images in a few minutes on current desktop platforms.

The APEX method assumes the image $g(x, y)$ to have been blurred by a restricted type of shift-invariant psf $h(x, y)$, one that can be expressed as a finite convolution product of 2-D radially symmetric Lévy stable probability density functions. Such so-called class **G** psfs include Gaussians, Lorentzians, and their convolutions. However, the class **G** also excludes defocus and motion blurs, and convolutions of such blurs with Gaussians and Lorentzians.

The synthetically blurred images $g(x, y)$ used in [9] were created by numerical convolution of sharp images $f(x, y)$ with class **G** psfs $h(x, y)$. Such blurred images necessarily obey the convolutional model $g(x, y) = h(x, y) \circledast f(x, y) + noise$, on which

*Mathematical and Computational Sciences Division, National Institute of Standards and Technology, Gaithersburg, MD 20899. (alfred.carasso@nist.gov).

the APEX method is predicated. In a real image, the blur need not be radially symmetric nor shift-invariant, and may otherwise be poorly approximated by an element of \mathbf{G} . More fundamentally, the blurring operator may not even be linear. Applicability of the APEX method to a given real image is far from obvious. Therefore, useful sharpening of any such image with an APEX-detected psf is always instructive.

Stable distributions are the natural generalization of the Gaussian distribution. Their theory was developed by Paul Lévy in the 1930's in connection with his work on the Central Limit Theorem, [13]. In the simplest radially symmetric case, these distributions are characterized by an exponent β , $0 < \beta \leq 1$, with $\beta = 1$ corresponding to the Gaussian distribution, and $\beta = 1/2$ corresponding to the Cauchy or Lorentzian distribution. Because stable distributions have infinite variance when $\beta < 1$, their appearance in physical contexts sometimes poses philosophical difficulties. In the present case, use of such psfs as the framework for the APEX method is motivated by the important role Lévy densities appear to play in numerous imaging systems. This is documented in section 2. When the APEX method is applied to a given image in the manner described below, a Lévy psf with a specific value of β is necessarily detected. That value of β may not be indicative of the actual physical process that created the image. This is true even if deblurring with the detected psf significantly improves the image. As shown in section 4, there are in general infinitely many distinct values of β that can produce useful reconstructions from the same blurred image. In some cases, the usefully enhanced image may not have been blurred by a class \mathbf{G} psf to begin with. In other cases, APEX processing does not significantly improve the image.

Below, we exhibit ten images where APEX processing provided noticeable improvement. These examples encompass such diverse imaging applications as astronomical, Landsat, and aerial images, MRI and PET brain scans, a scanning electron microscope image, a face image, and other types of interesting images. In some cases, the improvement is due primarily to an increase in contrast. In other cases, there is demonstrable sharpening of structural detail in addition to increased contrast. In all cases, the change in image quality is more than cosmetic, as APEX processing significantly alters the image Fourier transform. It is noteworthy that *low exponent* stable laws, with $\beta \ll 1/2$, were detected and used to deblur all of the images shown below. Such β -values are exceptional in physical contexts where radially symmetric Lévy densities appear. Whether or not these values have a physical origin cannot be ascertained in the present case. Moreover, the APEX detection procedure may not be well-founded. Nevertheless, the fact remains that the use of such psfs produced valuable restoration of real imagery from important fields of science and technology. To the author's knowledge, this application of sub-Cauchy stable laws in image processing is new and unanticipated.

In recent years, there has been considerable interest in image processing techniques that can be formulated as initial value problems in nonlinear partial differential equations. An instructive survey of these developments may be found in [10]. In particular, several novel approaches to image enhancement have been devised, based on integrating well-posed anisotropic nonlinear diffusion equations. In contrast, the APEX method centers around ill-posed continuation in linear fractional diffusion equations. The results obtained here appear to compare favorably with what is feasible with nonlinear methods, and they indicate the APEX method to be a useful addition to this developing methodology.

2. Imaging systems, Lévy processes, and the class \mathbf{G} . The occurrence and analysis of Lévy processes in the physical sciences are subjects of significant current

interest. See [1], [2], [4], [27], [29], [30], [33], and references therein. An important special case involves 2D radially symmetric Lévy stable densities $h(x, y)$, implicitly defined in terms of their Fourier transforms by

$$(1) \quad \hat{h}(\xi, \eta) \equiv \int_{R^2} h(x, y) e^{-2\pi i(\xi x + \eta y)} dx dy = e^{-\alpha(\xi^2 + \eta^2)^\beta}, \quad \alpha > 0, \quad 0 < \beta \leq 1.$$

The cases $\beta = 1$ and $\beta = 1/2$ correspond to Gaussian and Lorentzian (or Cauchy) densities respectively. For other values of β , $h(x, y)$ in (1) is not known in closed form. When $\beta = 1$, $h(x, y)$ has slim tails and finite variance. For $0 < \beta < 1$, $h(x, y)$ has fat tails and infinite variance. As noted in [33], there are examples in science where the occurrence of a stable law can be deduced from ‘first principles’ in terms of physical mechanisms that do not involve the parameter β explicitly. One such instance is the Holtsmark distribution describing the gravitational field of stars [13]. There, mathematical analysis reveals the value $\beta = 3/4$. Such cases must be distinguished from the many other cases where empirically obtained data with fat tails are *fitted* to a Lévy law, and the exponent β is *inferred* from these data. Given the limitations of physical measurements, such empirically established Lévy processes do not have the degree of scientific legitimacy that attends the Holtsmark distribution. The considerations of the present paper generally lie in this weaker scientific realm. Nevertheless, as will be seen below, techniques derived from such considerations turn out to be effective.

Image intensifiers, CCDs, and numerous other electronic devices are used in a wide variety of astronomical, industrial, biomedical, military, and surveillance imaging systems. See [3], [11], [12], [14], [26]. Each such device has a psf $h(x, y)$, characterizing that device’s imaging properties. The psf is a probability density function since it is non-negative and integrates to unity. Use of such a device to image an object $f(x, y)$ produces a blurred image $g(x, y) = h(x, y) \odot f(x, y)$, where \odot denotes convolution. An ideal device would have $h(x, y) = \delta(x, y)$. The Fourier transform $\hat{h}(\xi, \eta)$ of the psf is generally complex-valued and is called the *optical transfer function* (otf). The absolute value of the otf is the *modulation transfer function* (mtf).

In [31], it is noted that electron optical mtf’s are often nearly Gaussian in shape, and that this should be expected from the Central Limit Theorem, since the process of converting incoming signal photons into the final image that is observed on a screen involves many intermediate stages. However, it is also observed in [31] that when such mtf’s are fitted with Gaussians, the fitted curves often have *slimmer* tails than is the case in the true mtf’s.

A systematic study of electron optical mtf *measurements* is the subject of [17], [19], and [22]. There, the author claims the empirical discovery that a wide variety of electronic imaging devices, including phosphor screens and some types of photographic film, have otf’s $\hat{h}(\xi, \eta)$ that are well-described by (1) with $1/2 \leq \beta \leq 1$. For any given device, the values of α and β can be determined using specialized graph paper [23]. Other instances of electron optical stable laws are mentioned in [18], [21], and [25]. Analysis of the physical mechanisms responsible for such non Gaussian behavior is not included in these works. An understanding of such mechanisms may lead to the design of imaging devices with *low* values of β . The latter parameter affects the attenuation of high frequency information in the recorded image. Deconvolution of that image in the presence of noise, is generally better behaved at low values of β than it is at high values of β .

The characterization (1) is useful in other areas of optics. The otf for long-exposure imaging through atmospheric turbulence [15], is known to be given by (1)

with $\beta = 5/6$, and α determined by atmospheric conditions. Also, as shown in [20], the analytically known diffraction-limited otf for a perfect lens [32, p. 154], can be approximated over a wide frequency range by (1), with $\beta = 3/4$ and α a properly chosen function of the cutoff frequency.

The range of β values discussed above, namely $1/2 \leq \beta \leq 1$, mirrors that found in most other physical contexts where *symmetric* stable laws appear or are surmised. Values of $\beta \ll 1/2$ seem to be relatively rare in applications. Examples of such β values occur in [24], where mtf data for 56 different kinds of *photographic film* are analyzed. Good agreement is found when these data are fitted with (1), and the pairs (α, β) characterizing each of these 56 mtfs are identified. It is found that 36 types of film have mtfs where $1/2 \leq \beta \leq 1$. The remaining 20 types have mtfs with values of β in the range $0.265 \leq \beta \leq 0.475$.

We now consider imaging systems composed of various elements satisfying (1). Such systems might be used to image objects through a turbulent atmosphere or through other distorting media whose otfs obey (1). The resulting composite otf has the form

$$(2) \quad \hat{h}(\xi, \eta) = e^{-\sum_{i=1}^J \alpha_i (\xi^2 + \eta^2)^{\beta_i}}, \quad \alpha_i \geq 0, \quad 0 < \beta_i \leq 1.$$

Such an object corresponds to a *multifractal law* in [4]. We define the class **G** to be the class of all point spread functions $h(x, y)$ with Fourier transforms satisfying (2). We shall be interested in image deblurring problems

$$(3) \quad Hf \equiv \int_{R^2} h(x-u, y-v) f(u, v) du dv \equiv h(x, y) \otimes f(x, y) = g(x, y),$$

where $g(x, y)$ is the recorded blurred image, $f(x, y)$ is the desired unblurred image, and $h(x, y)$ is a known point spread function in class **G**. The blurred image $g(x, y)$ includes noise, which is viewed as a separate additional degradation,

$$(4) \quad g(x, y) = g_c(x, y) + n(x, y).$$

Here, $g_c(x, y)$ is the blurred image that would have been recorded in the absence of noise, and $n(x, y)$ represents the cumulative effects of all errors affecting final acquisition of the digitized array $g(x, y)$. The unique solution of (3) when the right hand side is $g_c(x, y)$, is the exact sharp image denoted by $f_c(x, y)$. Thus

$$(5) \quad h(x, y) \otimes f_c(x, y) = g_c(x, y).$$

3. Deblurring with the SECB method. The SECB method is a direct FFT-based image deblurring technique designed for equations of the form (3) when $h(x, y)$ is known and satisfies (2). Theoretical analysis of that method, along with error bounds and comparison with other methods, may be found in [5], [6], [7], [8]. Significantly, the method does not impose smoothness constraints on the unknown image $f(x, y)$. For class **G** psfs, we may define fractional powers H^t , $0 \leq t \leq 1$, of the convolution integral operator H in (3) as follows

$$(6) \quad H^t f \equiv \mathcal{F}^{-1} \left\{ \hat{h}^t(\xi, \eta) \hat{f}(\xi, \eta) \right\}, \quad 0 \leq t \leq 1.$$

Class **G** psfs are intimately related to diffusion processes, and solving (3) is equivalent to finding the initial value $u(x, y, 0) = f(x, y)$ in the *backwards in time* problem for

the generalized diffusion equation

$$(7) \quad \begin{aligned} u_t &= - \sum_{i=1}^J \lambda_i (-\Delta)^{\beta_i} u, \quad \lambda_i = \alpha_i (4\pi^2)^{-\beta_i}, \quad 0 < t \leq 1. \\ u(1) &= g(x, y). \end{aligned}$$

When $f(x, y)$ is known, $u(x, y, t) = H^t f$ is the solution of (7) at time t . The SECB method is a regularization method for solving the ill-posed problem (7) that takes into account the presence of noise in the blurred image data $g(x, y)$ at $t = 1$. The SECB deblurred image $f^\dagger(x, y)$ is obtained in closed form in Fourier space. With \bar{z} denoting the complex conjugate of z ,

$$(8) \quad \hat{f}^\dagger(\xi, \eta) = \frac{\overline{\hat{h}(\xi, \eta)} \hat{g}(\xi, \eta)}{|\hat{h}(\xi, \eta)|^2 + K^{-2} |1 - \hat{h}^s(\xi, \eta)|^2},$$

leading to $f^\dagger(x, y)$ upon inverse transforming. Here, the regularization parameters K, s are positive constants that depend on a-priori information. In practice, FFT algorithms are used to obtain $f^\dagger(x, y)$. This may result in individual pixel values that are negative, or that exceed 255, the maximum value in an 8-bit image. Accordingly, all negative values are reset to the value zero, and all values exceeding 255 are reset to the value 255. For 512×512 images, a single trial SECB restoration requires about 5 seconds of cpu time on current desktop workstations. We may also form and display

$$(9) \quad u^\dagger(x, y, t) = H^t f^\dagger(x, y),$$

for selected *decreasing* values of t lying between 1 and 0. This simulates *marching backwards in time* in (7), and allows *monitoring* the gradual deblurring of the image. As $t \downarrow 0$ the partial restorations $u^\dagger(x, y, t)$ become sharper. However, noise and other artifacts typically become more noticeable as $t \downarrow 0$. Gradual deblurring allows detection of features in the image before they become obscured by noise or ringing artifacts. Such marching backwards in time is an important element in the APEX method.

It should be noted that the class \mathbf{G} is only a small subclass of the class of *infinitely divisible* densities, [13]. The latter class includes multimodal non symmetric psfs, associated with linear diffusion equations more complex than (7). Detection of such psfs from blurred image data would require considerable extension of the APEX method discussed below.

4. Non uniqueness in blind deconvolution. Blind deconvolution of images is a mathematical problem that is not fully understood. Well-documented examples of the kinds of behavior that may occur are of particular interest. In this section, we highlight important non uniqueness aspects of that problem that are helpful in understanding the results of the APEX method. Let $f_c(x, y)$ be a given exact sharp image, let $h(x, y)$ be a Lévy point spread function, and let $g_c(x, y) = h(x, y) \otimes f_c(x, y)$. We shall show that given the blurred image $g_c(x, y)$, there are in general *many* point spread functions $h_i(x, y) \neq h(x, y)$ that deblur $g_c(x, y)$, producing *high quality* reconstructions $f_i(x, y) \neq f_c(x, y)$, with $h_i(x, y) \otimes f_i(x, y) \approx g_c(x, y)$.

The sharp 512×512 Sydney image $f_c(x, y)$ in Figure 1(A) was synthetically blurred by convolution with a Cauchy density $h(x, y)$ with $\alpha_0 = 0.075$, $\beta_0 = 0.5$. This produced the blurred image $g_c(x, y)$ in Figure 1(B). To avoid distractions caused by noise, the blurred image $g_c(x, y)$ in this experiment was computed and stored

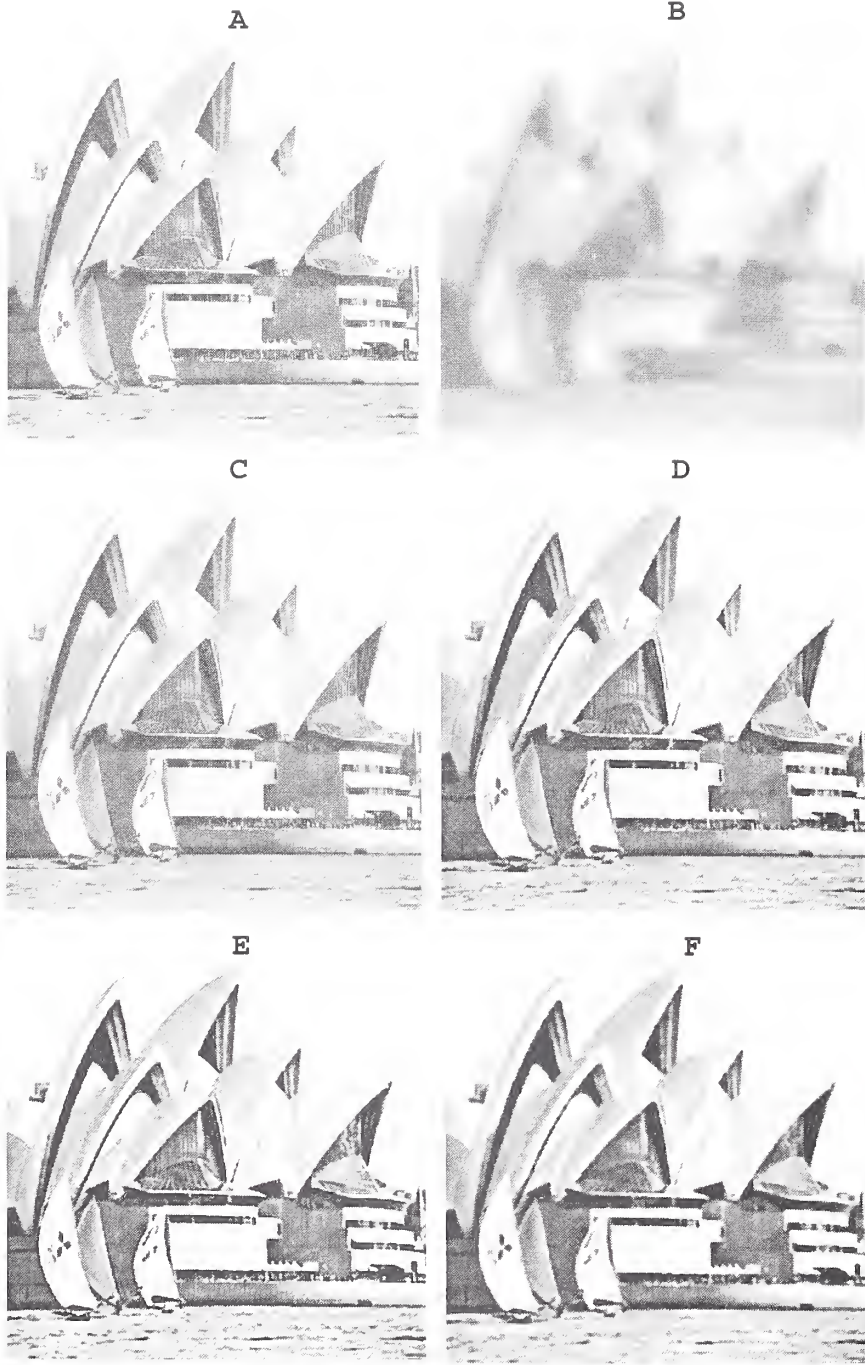


FIG. 1. *Non uniqueness in blind deconvolution. Distinct point spread functions exist that produce high quality reconstructions from same blurred image. (A) Original sharp 512×512 Sydney image. (B) Synthetically blurred Sydney image created by convolution with Lorentzian density with $\alpha_0 = 0.075$, $\beta_0 = 0.5$. Blurred image computed and stored in 64-bit precision. (C) Deblurring of image (B) using correct parameters $\alpha = 0.075$, $\beta = 0.5$. (D) Deblurring of image (B) using $\alpha = 0.1301264$, $\beta = 0.44298$. (E) Deblurring of image (B) using $\alpha = 0.1950345$, $\beta = 0.403889$. (F) Deblurring of image (B) using $\alpha = 0.2360994$, $\beta = 0.369666$. Notice that images (D), (E), and (F) were found using specific pairs (α, β) where $\alpha > \alpha_0$ and $\beta < \beta_0$. All deblurred images obtained using SECB procedure with $s = 0.001$ and $K = 10000$.*

in 64-bit precision. Deblurring this noiseless image with the correct psf values $\alpha = 0.075$, $\beta = 0.5$, produces Figure 1(C). This is in excellent visual agreement with $f_c(x, y)$ in Figure 1(A), as expected. However, the visual quality in Figures 1(D), 1(E), and 1(F) is generally as good as that in Figure 1(C). The latter three images were deblurred with Lévy densities with values (α, β) where $\alpha > \alpha_0$, $\beta < \beta_0$, and they differ from Figure 1(A) in contrast and brightness. All deblurred images were obtained using the SECB method with $s = 0.001$ and $K = 10000$. One dimensional cross sections of the four distinct psfs used in Figure 1 are displayed in Figure 2. These psfs also exhibit distinct heavy tail behavior not shown in Figure 2.

One can imagine four photographers, simultaneously photographing the identical scene depicted in Figure 1(A), yet producing the four distinct images shown in Figures 1(C), 1(D), 1(E), and 1(F), through use of different lenses, film, filters, exposures, printing, and the like. In practice, given only the blurred image in Figure 1(B), any one of these four restorations would be considered highly successful. Convolution of each reconstruction with its corresponding psf in Figure 2, reproduces the blurred image in Figure 1(B).

For any restoration $f(x, y)$ of the exact image $f_c(x, y)$ in Figure 1(A), and any norm $\| \cdot \|$, we can evaluate the relative error $\| f - f_c \| / \| f_c \|$. Define the discrete L^1 , L^2 , and H^m norms as follows

$$\begin{aligned}
 \| f \|_1 &= N^{-2} \sum_{x,y=1}^N |f(x, y)|, \\
 \| f \|_2 &= \left\{ N^{-2} \sum_{x,y=1}^N |f(x, y)|^2 \right\}^{1/2}, \\
 \| f \|_{H^m} &= \left\{ N^{-2} \sum_{\xi,\eta=1}^N (1 + \xi^2 + \eta^2)^m |f(\xi, \eta)|^2 \right\}^{1/2}.
 \end{aligned}
 \tag{10}$$

The relative errors in the L^1 , L^2 , H^1 and H^5 norms, for each of the four restorations in Figure 1, are shown in Table 1. As might be expected, image (C) is the closest to image (A) in each of these norms, since the correct psf values were used to obtain image (C) from image (B). It is also evident from Table 1 that the four restorations are distinct from one another, since they differ from image (A) by different amounts. Most important, the fact that image (E) is a significantly poorer approximation to image (A) in these norms than is image (C), *does not imply* that image (E) is an inaccurate representation of the visual scene depicted in image (A). Notice also that image (F) is not as sharp as image (E), although it is closer to image (A) in three of the four norms.

Iterative algorithms are the most common approach to blind deconvolution. Convergence proofs for such iterative procedures are seldom available. The above example illustrates some of the difficulties underlying any analysis of convergence. Such analysis should allow for the possibility of *infinitely many* useful limit points, while the mathematical characterization of such limit points is not obvious. Moreover, as is evident from Table 1 and has been known for some time, the use of L^p or H^m norms in assessing the visual quality of a reconstruction can be misleading.

5. Marching backwards in time and the APEX method. The APEX method is a blind deconvolution technique based on detecting class **G** psf signatures by appropriate 1-D Fourier analysis of the blurred image $g(x, y)$. The detected psf parameters are then input into the SECB algorithm to deblur the image. Let $f_c(x, y)$

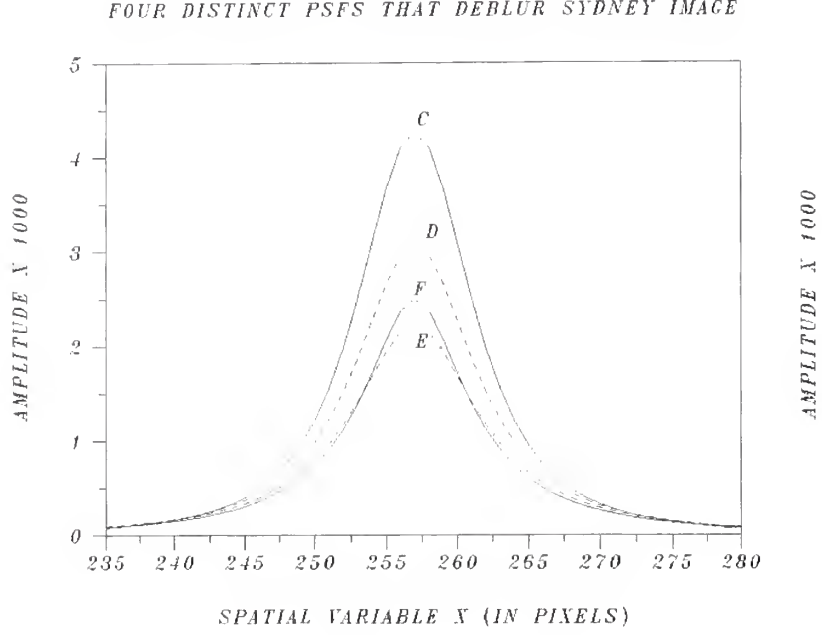


FIG. 2. Four distinct point spread functions that deblar image (B) in Figure 1. Curves C, D, E and F are 1-D cross sections of the 512×512 psfs that respectively produced images (C), (D), (E) and (F) in Figure 1. These psfs also exhibit distinct heavy tail behavior.

TABLE 1

Relative errors in various norms for the four deblurred images in Figure 1.

Restoration	Parameters α, β	L^1	L^2	H^1	H^5
Image (C)	$\alpha = 0.075, \beta = 0.500$	2.13 %	3.52 %	4.13 %	19.66 %
Image (D)	$\alpha = 0.130, \beta = 0.443$	6.63 %	8.37 %	8.67 %	21.11 %
Image (E)	$\alpha = 0.195, \beta = 0.404$	12.64 %	15.53 %	15.75 %	25.52 %
Image (F)	$\alpha = 0.236, \beta = 0.370$	12.54 %	15.08 %	15.31 %	26.17 %

be an exact sharp image as in (5). Since $f_e(x, y) \geq 0$

$$(11) \quad |\hat{f}_e(\xi, \eta)| \leq \int_{R^2} f_e(x, y) dx dy = \hat{f}_e(0, 0) = \sigma > 0.$$

Also, since $g_e(x, y) = h(x, y) \odot f_e(x, y)$ and $h(x, y)$ is a probability density,

$$(12) \quad \hat{g}_e(0, 0) = \int_{R^2} g_e(x, y) dx dy = \int_{R^2} f_e(x, y) dx dy = \hat{f}_e(0, 0) = \sigma > 0.$$

Using σ as a normalizing constant, we may normalize Fourier transform quantities $\hat{q}(\xi, \eta)$ by dividing by σ . Let

$$(13) \quad \hat{q}^*(\xi, \eta) = \hat{q}(\xi, \eta)/\sigma,$$

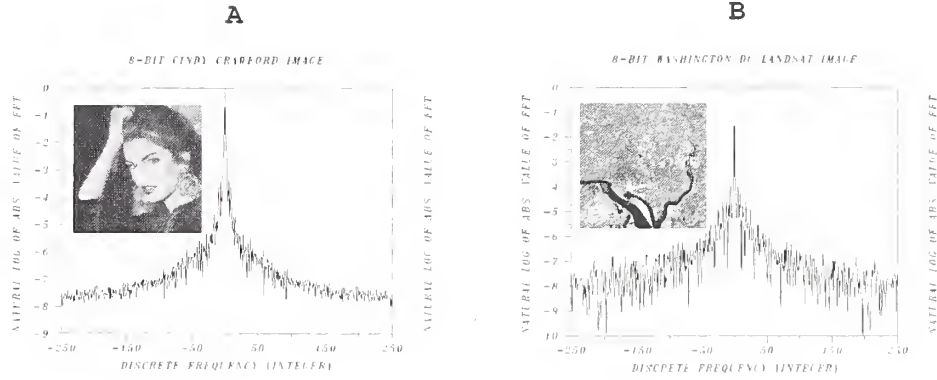


FIG. 3. Behavior of normalized Fourier transform in types of blurred images $g(x, y)$ considered in present paper. (A) $\log |\hat{g}^*(\xi, 0)|$ in Cindy Crawford image. (B) $\log |\hat{g}^*(\xi, 0)|$ in Washington DC Landsat image. While local behavior is highly oscillatory, global behavior is generally monotone decreasing and convex.

denote the normalized quantity. The function $|\hat{f}_e^*(\xi, \eta)|$ is highly oscillatory, and $0 \leq |\hat{f}_e^*| \leq 1$. Since $f_e(x, y)$ is real, its Fourier transform is conjugate symmetric. Therefore, the function $|\hat{f}_e^*(\xi, \eta)|$ is symmetric about the origin on any line through the origin in the (ξ, η) plane. The same is true for the blurred image data $|\hat{g}^*(\xi, \eta)|$.

All blurred images in this and the next section are of size 512×512 and quantized at 8-bits per pixel. For any blurred image $g(x, y)$, the discrete Fourier transform is a 512×512 array of complex numbers, which we again denote by $g(\xi, \eta)$ for simplicity. The 'frequencies' ξ, η are now integers lying between -256 and 256 , and the zero frequency is at the center of the transform array. This ordering is achieved by pre-multiplying $g(x, y)$ by $(-1)^{x+y}$. We shall be interested in the values of such transforms along single lines through the origin. The discrete transforms $|\hat{g}^*(\xi, 0)|$, and $|\hat{g}^*(0, \eta)|$ are immediately available. Image rotation may be used to obtain discrete transforms along other directions. All 1-D Fourier domain plots shown in this paper are taken along the axis $\eta = 0$ in the (ξ, η) plane. In these plots, the zero frequency is at the center of the horizontal axis, and the graphs are necessarily symmetric about the vertical line $\xi = 0$. Examples of such plots are shown in Figures 3, 5, and 10.

The class of blurred images $g(x, y)$ considered in the present paper can be described in terms of the behavior of $\log |\hat{g}^*(\xi, \eta)|$ along lines through the origin in the (ξ, η) plane. While local behavior is highly oscillatory, global behavior is generally monotone decreasing and *convex*. This is shown in Figure 3 for two typical images, along the line $\eta = 0$. In [9], a large class of images with that property was exhibited, the class W. The blurred images considered here may be loosely characterized as being in class W. Not all blurred images may be so characterized. For example, if the Cindy Crawford image $g(x, y)$ in Figure 3(A) were convolved with a wide Gaussian psf to form a new blurred image $g_1(x, y)$, global behavior in $\log |\hat{g}_1^*(\xi, 0)|$, away from the origin, would be monotone decreasing and *concave*. Application of the APEX method to several concave examples is discussed in [9]. Convolution of Figure 3(A) with a defocus psf produces a different kind of blurred image $g_2(x, y)$, and global behavior in $\log |\hat{g}_2^*(\xi, 0)|$ is neither concave nor convex. Instead, there is a regular pattern of sharp singularities corresponding to successive zeroes of the defocus of. Use of the APEX method in the manner to be described below, is intended only for

blurred images with Fourier behavior analogous to that shown in Figure 3.

The APEX method is based on the following observations. In the basic relation

$$(14) \quad g(x, y) = h(x, y) \odot f_e(x, y) + n(x, y),$$

we may safely assume that the noise $n(x, y)$ satisfies

$$(15) \quad \int_{R^2} |n(x, y)| dx dy \ll \int_{R^2} f_e(x, y) dx dy = \sigma > 0,$$

so that,

$$(16) \quad |\hat{n}^*(\xi, \eta)| \ll 1.$$

Consider the case where the otf is a pure Lévy density $h(\xi, \eta) = e^{-\alpha(\xi^2 + \eta^2)^\beta}$. Since $g = g_e + n$

$$(17) \quad \log |\hat{g}^*(\xi, \eta)| = \log |e^{-\alpha(\xi^2 + \eta^2)^\beta} \hat{f}_e^*(\xi, \eta) + \hat{n}^*(\xi, \eta)|.$$

Let $\Omega = \{(\xi, \eta) \mid \xi^2 + \eta^2 \leq \omega^2\}$ be a neighborhood of the origin where

$$(18) \quad e^{-\alpha(\xi^2 + \eta^2)^\beta} |\hat{f}_e^*(\xi, \eta)| \gg |\hat{n}^*(\xi, \eta)|.$$

Such an Ω exists since (18) is true for $\xi = \eta = 0$ in view of (16). The radius $\omega > 0$ of Ω decreases as α and n increase. For $(\xi, \eta) \in \Omega$ we have

$$(19) \quad \log |\hat{g}^*(\xi, \eta)| \approx -\alpha(\xi^2 + \eta^2)^\beta + \log |\hat{f}_e^*(\xi, \eta)|.$$

Because of the radial symmetry in the psf, it is sufficient to consider (19) along a single line through the origin in the (ξ, η) plane. Choosing the line $\eta = 0$, we have

$$(20) \quad \log |\hat{g}^*(\xi, 0)| \approx -\alpha|\xi|^{2\beta} + \log |\hat{f}_e^*(\xi, 0)|, \quad |\xi| \leq \omega.$$

Some type of a-priori information about $f_e(x, y)$ is necessary for blind deconvolution. In (20), knowledge of $\log |\hat{f}_e^*(\xi, 0)|$ on $|\xi| \leq \omega$ would immediately yield $-\alpha|\xi|^{2\beta}$ on that interval. Moreover, any other line through the origin could have been used in (19). However, such detailed knowledge is unlikely in practice. The APEX method seeks to identify a useful psf from (20) without prior knowledge of $\log |\hat{f}_e^*(\xi, 0)|$. The method assumes instead that $f_e(x, y)$ is a recognizable object, and typically requires several interactive trials before locating a suitable psf. As previously noted, such trial SECB restorations are easily obtained. Here, prior information about $f_e(x, y)$ is disguised in the form of user recognition or rejection of the restored image, and that *constraint* is applied at the end of the reconstruction phase, rather than at the beginning of the detection phase.

In the absence of information about $\log |\hat{f}_e^*(\xi, 0)|$, we replace it by a negative constant $-A$ in (20). For any $A > 0$, the approximation

$$(21) \quad \log |\hat{g}^*(\xi, 0)| \approx -\alpha|\xi|^{2\beta} - A,$$

is not valid near $\xi = 0$, since the curve $u(\xi) = -\alpha|\xi|^{2\beta} - A$, has $-A$ as its apex. Choosing a value of $A > 0$, we best fit $\log |\hat{g}^*(\xi, 0)|$ with $u(\xi) = -\alpha|\xi|^{2\beta} - A$ on the interval $|\xi| \leq \omega$, using nonlinear least squares algorithms. The resulting fit is close

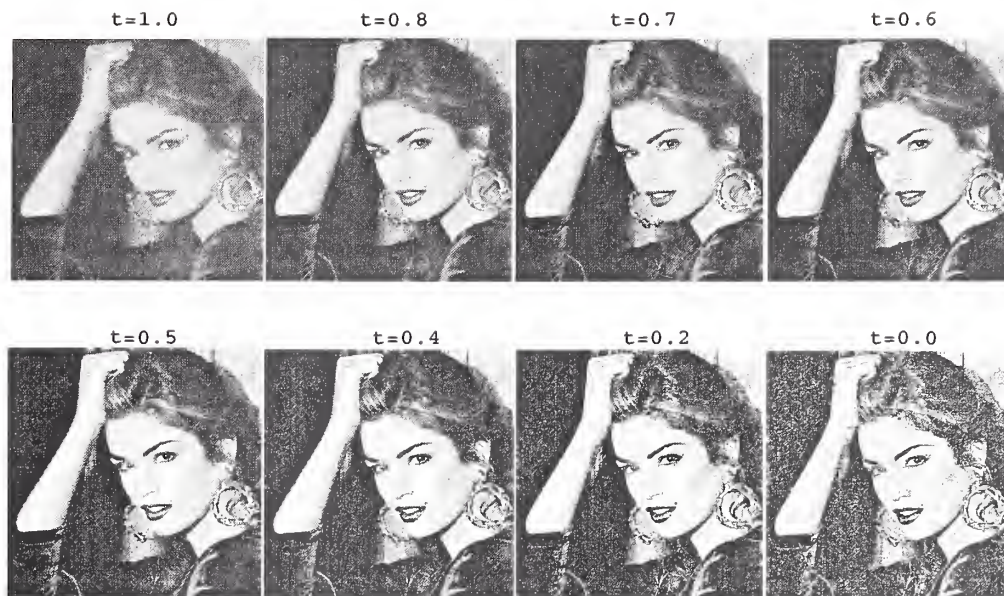


FIG. 1. Enhancement of Cindy Crawford image by marching backwards from $t = 1$ with APEX detected psf. Image sequence shows gradual increase in contrast as t decreases. Undesirable artifacts at $t = 0$ indicate continuation backwards in time has proceeded too far. Best results are highly subjective in this case, but probably occur at some $t > 0.5$. Note sharpness of earrings near $t = 0.5$.

only for ξ away from the origin. The returned values for α and β are then used in the SECB deblurring algorithm. Different values of A return different pairs (α, β) . Experience indicates that useful values of A generally lie in the interval $2 \leq A \leq 6$. Increasing the value of A decreases the curvature of $u(\xi)$ at $\xi = 0$, resulting in a larger value of β together with a smaller value of α . A value of $A > 0$ that returns $\beta > 1$ is clearly too large, as $\beta > 1$ is impossible for probability density functions [13]. Decreasing A has the opposite effect, producing lower values of β and higher values of α . As a rule, deconvolution is better behaved at lower values of β than it is when $\beta \approx 1$. A significant observation is that *an image blurred with a pair (α_0, β_0) can often be successfully deblurred with an appropriate pair (α, β) , where $\alpha > \alpha_0$ and $\beta < \beta_0$* . Examples of this phenomenon were shown in Figure 1 in connection with the blurred Sydney image. An effective interactive framework for performing the above least squares fitting is the *fit* command in *DATAPLOT* [16]. This is a high-level English-syntax graphics and analysis software package developed at the National Institute of Standards and Technology. This software tool was used throughout this paper.

The following version of the APEX method, using the SECB *marching backwards in time* option (9), has been found useful in a variety of image enhancement problems where the image $g(x, y)$ is such that $\log |\hat{g}^*(\xi, 0)|$ is generally globally monotone decreasing and convex, as shown in Figure 3. Choose a value of $A > 0$ in (21) such that the least squares fit develops a slight *cusp* at $\xi = 0$. Using the returned pair (α, β) in the SECB method, obtain a sequence $u^\dagger(x, y, t)$ of partial restorations as t decreases from $t = 1$, as illustrated in the Cindy Crawford sequence in Figure 4. With a good choice of A , high quality restorations will be found at positive values of

t , and these will gradually deteriorate as $t \downarrow 0$. Typically, the restoration at $t = 0$ will exhibit undesirable artifacts, indicating that continuation backwards in time has proceeded *too far* in (7). Terminating the continuation at some appropriate $t = t_1 > 0$, is equivalent to rescaling the value of α without changing the value of β . If the pair (α, β) produces a high quality restoration at $t = t_1 > 0$, the pair (α_1, β) , where $\alpha_1 = (1 - t_1)\alpha$, will produce the same quality results at $t = 0$. In general, there will be many values of A in (21) returning pairs (α, β) that produce good reconstructions at some $t_{\alpha\beta} > 0$. A large number of distinct pairs (α^*, β^*) can thus be found that produce useful, but distinct, results at $t = 0$. Indeed, this is the process that was used to obtain the four psfs shown in Figure 2.

We have been assuming $h(\xi, \eta)$ to be a pure Lévy of in (14). For more general class \mathbf{G} of (2), we may still use the approximation $\log |\hat{g}^*(\xi, 0)| \approx -\alpha|\xi|^{2\beta} - A$, and apply the same technique to extract a suitable pair (α, β) from the blurred image. Here, the returned APEX values may be considered average values for the α_i, β_i in (2), producing a single pure Lévy of approximating the composite of.

6. Application to real images. The developments in sections 2 through 5 are predicated on two assumptions. The first assumption is that the blurred image $g(x, y)$ obeys the simple convolution equation (3) rather than a more general, possibly nonlinear, integral equation

$$(22) \quad Hf = \int_{R^2} h(x, y, u, v, f(u, v)) du dv = g(x, y)$$

In addition to linearity, (3) implies that the blur is isoplanatic. The second assumption is that the point spread function $h(x, y)$ belongs to a restricted class of unimodal, radially symmetric, probability density functions, the class \mathbf{G} defined in (2). In [9], successful blind deconvolution of *synthetically blurred* images, with added noise, was demonstrated. Such synthetically blurred images necessarily obey (2) and (3).

The applicability of the preceding theory to real blurred images is by no means assured. Deviations from linearity, isoplanatism, unimodality, and radial symmetry are possible. Moreover, the class \mathbf{G} excludes motion and defocus blurs. In addition, the types and intensities of noise processes in real images may differ fundamentally from the noise models typically used in numerical experiments. Therefore, only limited success on a narrow class of images can be expected in real applications.

The examples discussed below involve images obtained from multiple sources using diverse imaging modalities. Some of these images have been used as test images in the literature. In this paper, each of these images is assumed to have been blurred by some unknown process, and we seek to improve visual quality by APEX processing. All images are of size 512×512 and quantized at 8 bits per pixel.

Our first example is a well-known English village image denoted by $g(x, y)$, and shown in Figure 5(A) together with $\log |\hat{g}^*(\xi, 0)|$ on $|\xi| \leq 250$. The plot displays globally convex monotone behavior. In Figure 5(B), the APEX fit of $\log |\hat{g}^*(\xi, 0)|$ with $u(\xi) = -\alpha|\xi|^{2\beta} - A$, on the interval $|\xi| \leq 200$, is shown. With $A = 3.75$, the fit develops a cusp at $\xi = 0$ and returns $\alpha = 0.251274$, $\beta = 0.242246$. With these psf parameters, SECB deblurring using $s = 0.01$, $K = 1300$, and continuation backwards in time terminated at $t = 0.5$, produces Figure 6(B). This is compared with the original in Figure 6(A).

The extent of sharpening in Figure 6(B) becomes evident when zooming on selected parts of the image. In Figure 7, rooflines on the first three houses are compared

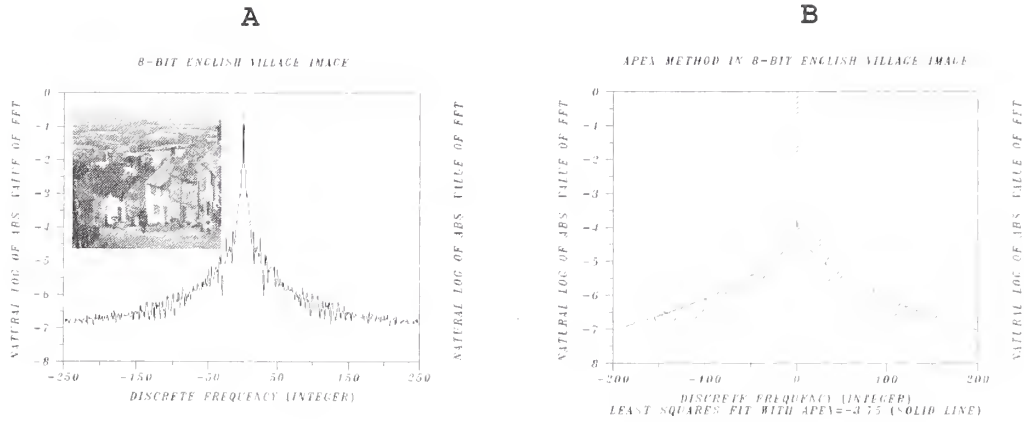


FIG. 5. APEX method of psf detection. (A) $\log |\hat{g}^*(\xi, 0)|$ on $|\xi| \leq 250$ in 8-bit English village image. (B) Least squares fit of $\log |\hat{g}^*(\xi, 0)|$ with $n(\xi) = -\alpha |\xi|^{2\beta} - 3.75$ on $|\xi| \leq 200$, develops cusp at $\xi = 0$ and returns $\alpha = 0.251274$, $\beta = 0.242246$.



FIG. 6. Enhancement of English village image. (A) Original 8-bit image. (B) SECB deblurred image using $s = 0.01$, $K = 1300$, with APEX detected values $\alpha = 0.251271$, $\beta = 0.242246$, and continuation backwards in time terminated at $t = 0.5$.

before and after APEX processing. There is noticeable enhancement of structural detail in the roof shingles and stone fronts of the three houses in Figure 7(B). In Figure 8(B), Holstein cows grazing in the meadow, not previously identifiable, are clearly visible. So are individual chimney bricks. In Figure 9(B), buildings in the distance, not readily noticed in Figure 9(A), become well-defined.

It should be noted that use of a different value of A , and/or a different neighborhood of the origin Ω in Figure 5(B), may return a different psf pair (α, β) . In

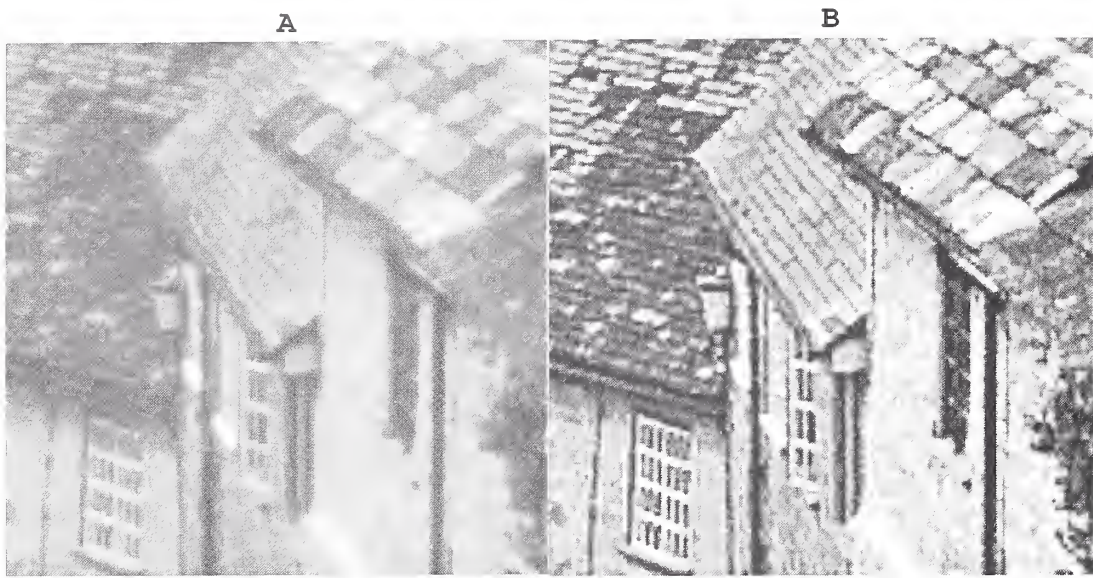


FIG. 7. *Extent of sharpening in English village scene becomes evident when zooming on selected parts of the image. (A). Rooflines in original image. (B). Rooflines in enhanced image.*

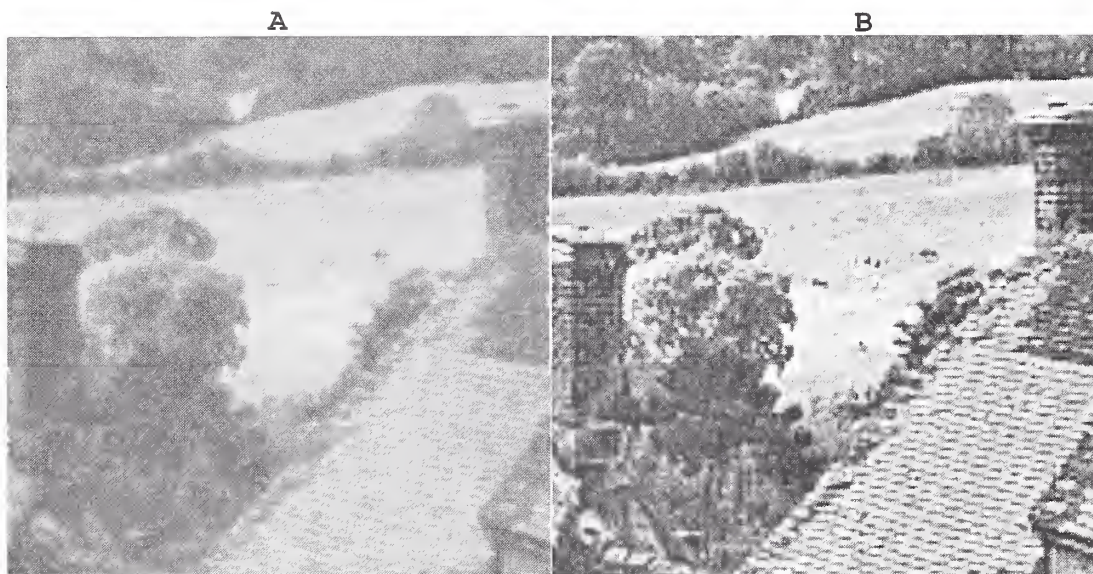


FIG. 8. *Extent of sharpening in English village scene becomes more evident with zooming. Holstein cows grazing in meadow in image (B) are not readily identifiable in image (A).*

that case, backwards continuation in the SECB method may need to be terminated at some other value of t to obtain the best image. However, with good choices of A and Ω , the latter image would again be a high quality representation of the visual scene in Figure 6(B), while differing from Figure 6(B) at individual pixels. This is the non uniqueness phenomenon previously discussed in connection with the Sydney

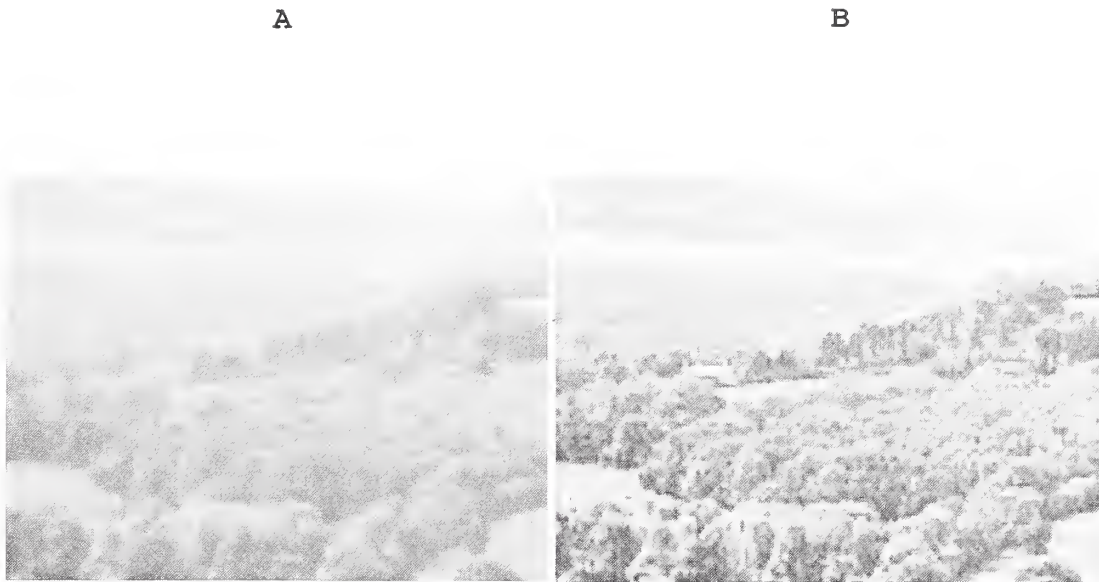


FIG. 9. Extent of sharpening in English village image becomes more evident with zooming. Enhanced image (B) shows buildings in distance not immediately apparent in original image (A).

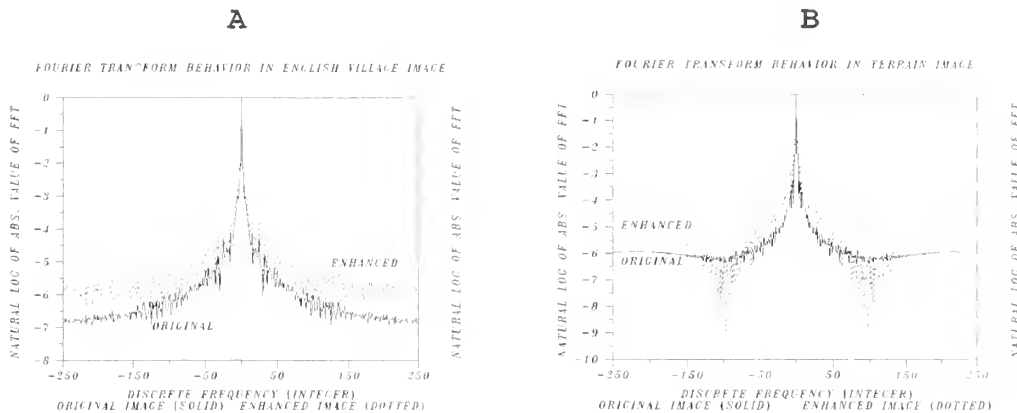


FIG. 10. APEX processing significantly alters Fourier transform behavior. (A) English village image before and after processing. (B) F15 terrain image in Figure 12 before and after processing. Behavior shown in (B) is exceptional. All other examples in present paper conform with behavior shown in (A).

image in Figure 1.

Deconvolution of Figure 6(A) with the above APEX-detected psf significantly alters its Fourier transform. As shown in Figure 10(A), the Fourier transform in Figure 6(B) (dashed curve), decays less rapidly as $|\xi|$ increases than was the case in the original Figure 6(A) (solid curve). Evidently, APEX processing amplifies high frequency image components in a stable coherent fashion, resulting in the overall improvements visible in Figures 6 through 9. The 'before and after' Fourier transform



FIG. 11. *Enhancement of boat image. APEX method with $A = 4.0$ on $|\xi| \leq 250$, yields $\alpha = 0.518155$, $\beta = 0.215083$. Using these parameters with $s = 0.01$, $K = 1300$, and backwards continuation terminated at $t = 0.5$, SECB method applied to image (A) produces image (B). Number 7 2 7 on side of boat in image (B) was not easily identifiable in image (A).*

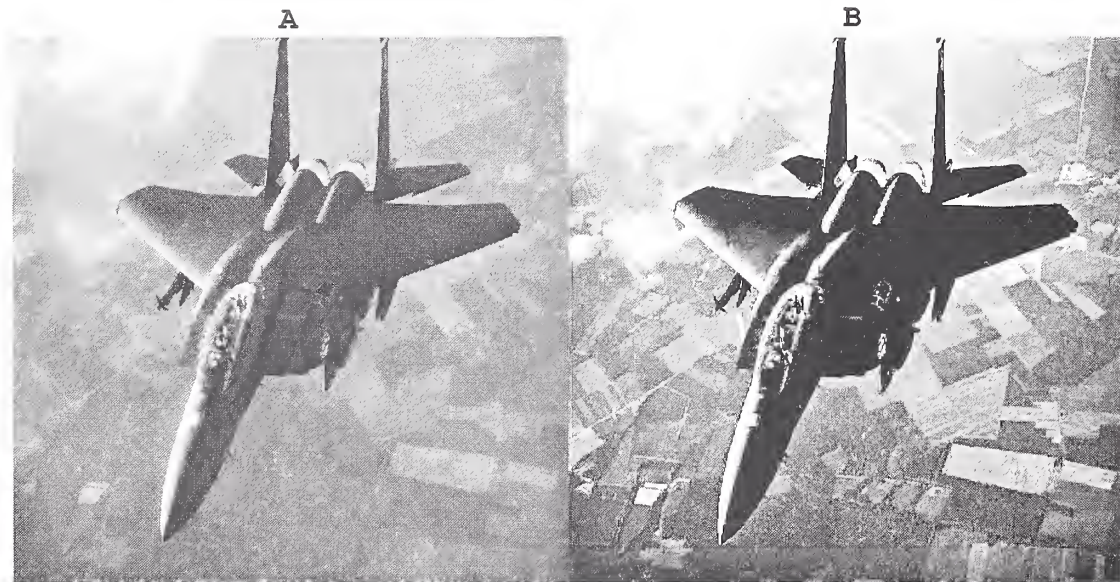


FIG. 12. *Striking enhancement of terrain features in F15 image. APEX method with $A = 3.5$ on $|\xi| \leq 250$, yields $\alpha = 0.856096$, $\beta = 0.107289$. Using these parameters with $s = 0.01$, $K = 1000$, and backwards continuation terminated at $t = 0.25$, SECB method applied to image (A) produced image (B). Condensation trails behind aircraft in image (B) not immediately evident in image (A).*

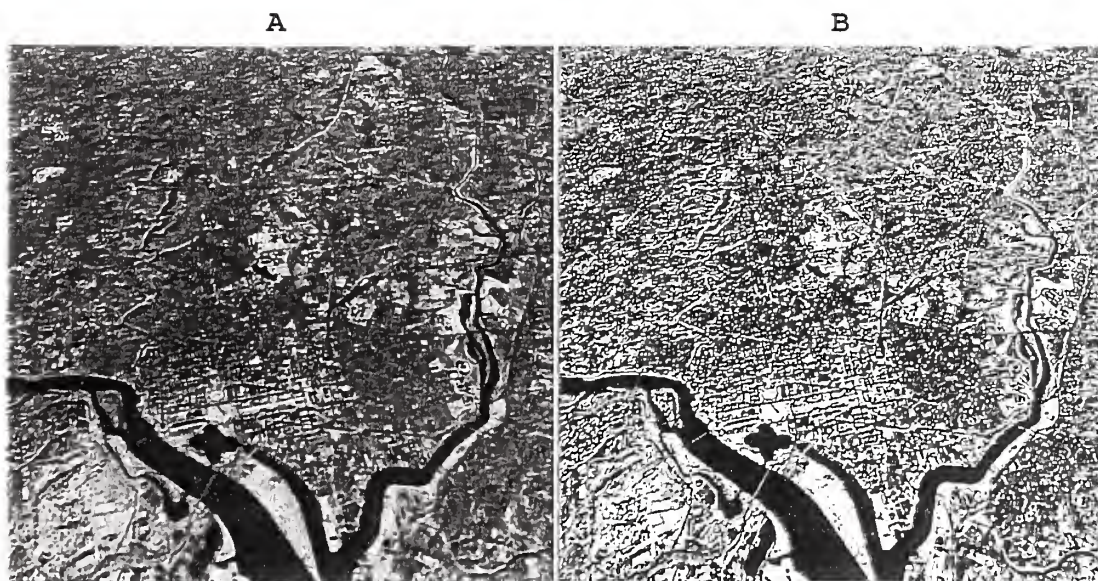


FIG. 13. Enhancement of Washington DC Landsat image. APEX method with $A = 4.25$ on $|\xi| \leq 250$, yields $\alpha = 0.540825$, $\beta = 0.182410$. Using these parameters with $s = 0.01$, $K = 1300$, and backwards continuation terminated at $t = 0.5$, SECB method applied to image (A) produced image (B). Increased resolution in image (B) improves definition of several landmarks and thoroughfares.

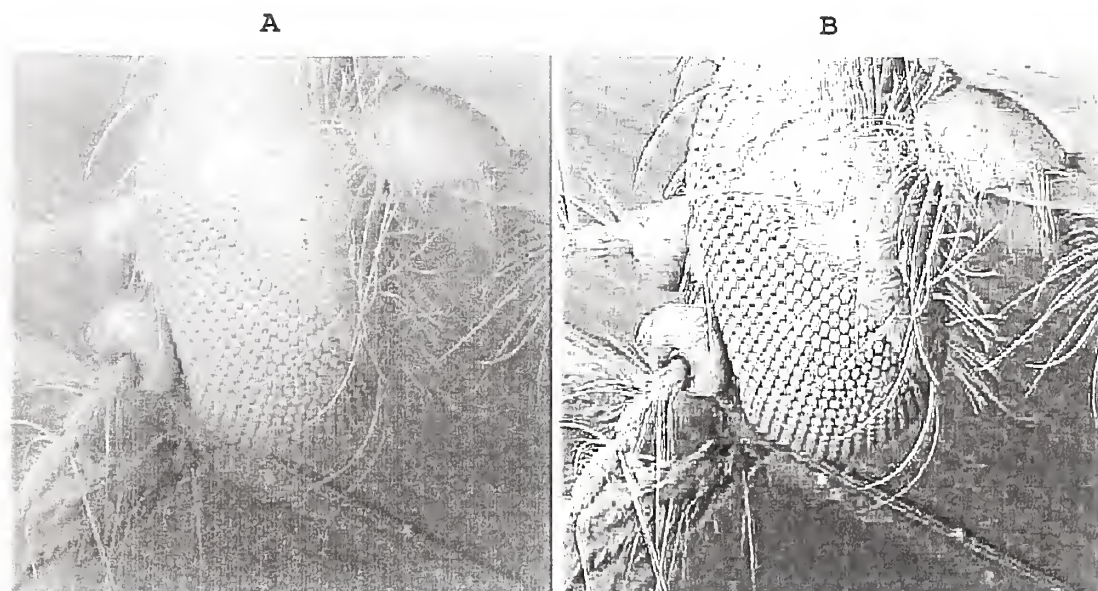


FIG. 14. Enhancement of scanning electron microscope image of a mosquito's head showing compound eye. APEX method with $A = 4.0$ on $|\xi| \leq 250$, yields $\alpha = 0.734259$, $\beta = 0.156963$. Using these parameters with $s = 0.001$, $K = 10$, and backwards continuation terminated at $t = 0.4$, SECB method applied to image (A) produced image (B). APEX processing enhances contrast and brings eye into sharper focus.



FIG. 15. Enhancement of sagittal MRI brain image. APEX method with $A = 4.0$ on $|\xi| \leq 250$, yields $\alpha = 0.333267$, $\beta = 0.209416$. Using these parameters with $s = 0.01$, $K = 1300$, and backwards continuation terminated at $t = 0.35$, SECB procedure applied to image (A) produced image (B). APEX processing noticeably improves feature definition in areas between two and four o'clock.

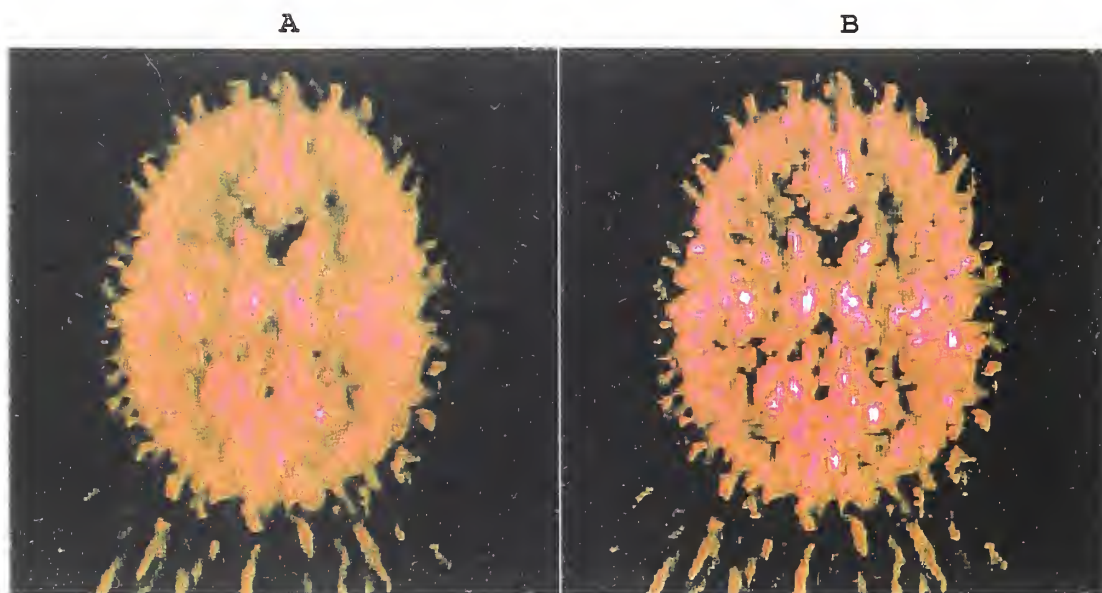


FIG. 16. Enhancement of transverse PET brain image. APEX method with $A = 5.0$ on $|\xi| \leq 250$, yields $\alpha = 0.198931$, $\beta = 0.284449$. Using these parameters with $s = 0.001$, $K = 5.0$, and backwards continuation terminated at $t = 0.6$, SECB procedure applied to image (A) produced image (B). Bright spots in enhanced image (B), indicating areas of the brain responding to applied external stimuli, are barely visible in original image (A).

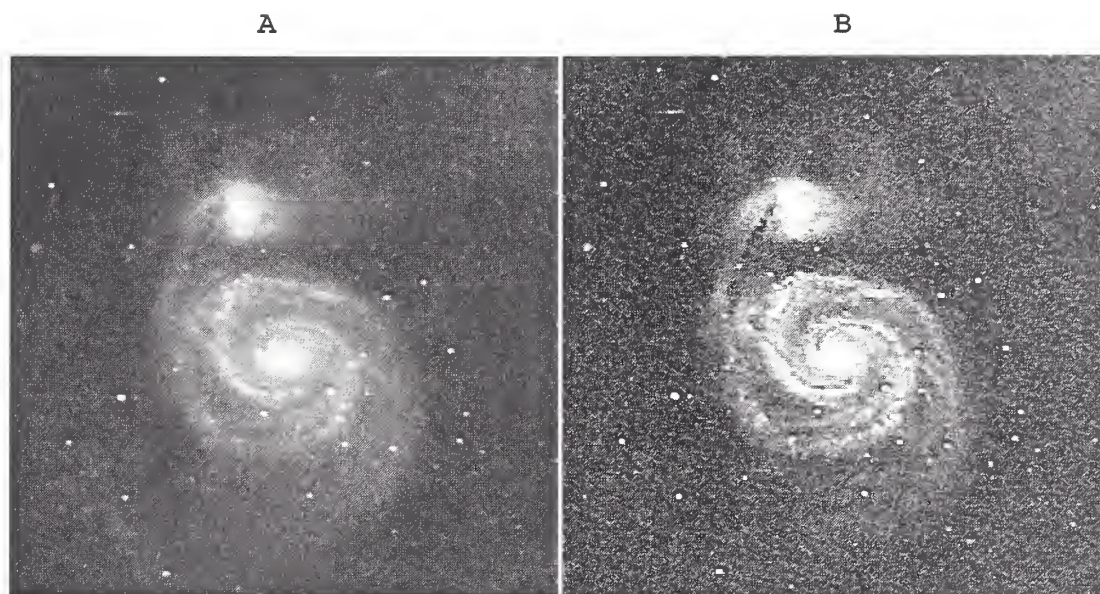


FIG. 17. *Enhancement of Whirlpool Galaxy (M51) image. APEX method with $A = 4.0$ on $|\xi| \leq 250$, yields $\alpha = 0.451615$, $\beta = 0.221955$. Using these parameters with $s = 0.001$, $K = 5.0$, and backwards continuation terminated at $t = 0.5$, SECB applied to image (A) produced image (B). APEX processing increases resolution and enhances luminosity in spiral arms and galactic cores.*

pattern shown in Figure 10(A) occurs in every example discussed in this paper, with the exception of the F15 image in Figure 12. The anomalous behavior in that case is shown in Figure 10(B).

The next example is the boat image in Figure 11(A). With $A = 4.0$, the APEX fit on $|\xi| \leq 250$ returned $\alpha = 0.518155$, $\beta = 0.215083$. Using these values in the SECB method, with $s = 0.01$, $K = 1300$, and continuation terminated at $t = 0.5$, produced Figure 11(B). Enhancement has now rendered visible the number 7 2 7 on the left side of the boat. Other identifiable details include the stripe along the left trouser leg of the man on the ground, the lettering on the sign hanging from the boat to his right, and part of the stone work and stairway to the left of the lighthouse.

The F15 plane image in Figure 12(A) is another interesting example. The aim here is to enhance the background terrain. With $A = 3.5$, the APEX fit on $|\xi| \leq 250$ develops a cusp at $\xi = 0$ and returns $\alpha = 0.856096$, $\beta = 0.107289$. Using these values in the SECB method, with $s = 0.01$, $K = 1000$, and backwards continuation terminated at $t = 0.25$, produces rather striking enhancement of the ground features in Figure 12(B). This example is noteworthy on two counts: the exceptionally low value of β detected by the APEX method, and the previously mentioned unexpected Fourier behavior shown in Figure 10(B).

Beginning with Figure 1, all of the examples discussed so far involve images of familiar objects. This allows for relatively easy evaluation of the results of APEX processing. The next five examples involve less familiar objects. Moreover, fine details visible on a modern high resolution computer screen are sometimes lost in the printing process. Consequently, improvements in image quality in some of the next examples may seem less obvious than in previous examples. At the same time, the performance of the APEX method in reconstructing real details of familiar objects,

provides a measure of confidence in the results obtained when that method is applied to unfamiliar objects.

Figure 13(A) is a Landsat image of the Washington DC area. With $A = 4.25$, the APEX fit on $|\xi| \leq 250$ returns $\alpha = 0.540825$, $\beta = 0.182410$. Using these parameters in the SECB method with $s = 0.01$, $K = 1300$, and continuation terminated at $t = 0.5$, produces Figure 13(B). There is a significant increase in resolution in Figure 13(B), which improves definition of several landmarks and thoroughfares. The Washington Monument, the bridges over the Potomac, Pennsylvania and Maryland Avenues radiating from the Capitol, Massachusetts Avenue to the north, and Virginia Avenue and the Southeast Freeway to the south, are some of the features that are more easily identified in the enhanced image.

Figure 14(A) is a scanning electron microscope image of a mosquito's head. A prominent feature is the insect's compound eye. With $A = 4.0$, the APEX fit on $|\xi| \leq 250$ yields $\alpha = 0.734259$, $\beta = 0.156963$. Using these values in the SECB method with $s = 0.001$, $K = 10.0$, and backwards continuation terminated at $t = 0.4$, produces Figure 14(B). Evidently, APEX processing results in significant overall improvement. In particular, the eye appears in much sharper focus.

The sagittal MRI brain image in Figure 15(A) has been used as a test *sharp* image in previous publications. In [5] and [7], synthetically blurred versions of that sharp image were used in a comparative evaluation of restoration algorithms when the psf is *known*. Here, we consider further sharpening the sharp image by blind deconvolution. With $A = 4.0$, the APEX fit on $|\xi| \leq 250$ returns $\alpha = 0.333267$, $\beta = 0.209416$. Using these parameters in the SECB procedure with $s = 0.01$, $K = 1300$, and continuation terminated at $t = 0.35$, produced the image in Figure 15(B). Substantial improvement is apparent over the whole image. In the sector between two and four o'clock in particular, sharpening of structural detail significantly improves feature definition.

In PET imaging, a positron emitting radionuclide is injected into the patient and used to tag glucose molecules in their course through the brain. The metabolic rate of glucose is a key parameter that measures cerebral function and reflects the extent to which regions of the brain are working or failing to work. Performing specific mental tasks activates various parts of the brain, causing increased glucose uptake and hence increased positron emission. Centers of activity translate into relatively bright spots in the PET image. However, blurring by the scanner psf tends to average out such relative differences, resulting in loss of contrast. Figure 16(A) is a PET image of a transverse slice through the brain. Blind deconvolution is used to enhance that image. With $A = 5.0$, the APEX fit on $|\xi| \leq 250$ returns $\alpha = 0.198931$, $\beta = 0.284449$. Using these parameters in the SECB method with $s = 0.001$, $K = 5.0$, and backwards continuation terminated at $t = 0.6$, produces Figure 16(B). Note that both images in Figure 16 show identical features, but contrast has been increased in the APEX processed image, with some regions becoming darker while others have become lighter. In particular, several bright spots appear in Figure 16(B) that were not readily apparent in the original image.

Our last example is the Whirlpool galaxy (M51) in Figure 17(A). With $A = 4.0$, the APEX fit on $|\xi| \leq 250$ yields $\alpha = 0.451615$, $\beta = 0.221955$. Using these values in the SECB method with $s = 0.001$, $K = 5.0$, and backwards continuation terminated at $t = 0.5$, produced Figure 17(B). In the enhanced image, the spiral arms are more luminous and better defined, and the luminous cores are larger in both the spiral galaxy and its companion. The dark connecting arm between the two galaxies is also more clearly defined. These enhancements are due to a change in Fourier transform

behavior brought about by deconvolution with the APEX-detected psf. This change in Fourier behavior is similar to that shown in Figure 10(A), although it is more pronounced. A concomitant effect of deconvolution is amplification of data noise, which now becomes visible against the dark background in Figure 17(B).

Clearly, in this galaxy image as in the preceding PET image, there is no way of knowing whether or not the enhanced image conforms with reality. Conceivably, the increased luminosity in Figure 17(B) may be exaggerated. However, the bright areas along the galactic arms in Figure 17(B), as well as the bright spots in Figure 16(B), did not materialize spontaneously. These areas must have been just below some brightness threshold in the original image, and APEX processing has served the very useful purpose of revealing their presence. If such areas appear overenhanced, this can be corrected by repeating the SECB procedure and terminating continuation at *higher* values of t .

7. Concluding remarks. Setting aside all theoretical considerations, a practical enhancement technique has been presented that can sharpen significant classes of images, originating from diverse imaging modalities. One important feature of the above approach is its fast implementation on desktop platforms. Even with large size images, numerous trial restorations can be accomplished in a few minutes of cpu time. This makes for easy fine tuning of parameters. Whether or not APEX processing significantly improves a given image can generally be quickly decided. Once improvement is detected, fine tuning must be used to obtain optimal results. Here, another important feature of the APEX method plays a useful role. This is the marching backwards in time option characteristic of class **G** psfs, which allows for deconvolution to be performed in *slow motion*. Robustness is a third important property of the APEX method, allowing detection of multiple psfs capable of significant sharpening. This substantially increases the probabilities of finding a useful candidate.

On the theoretical side, this paper raises new questions. The first of these is the existence of several useful psfs, as demonstrated in the Sydney image in Figure 1. This phenomenon warrants further investigation. A second question concerns the important role Lévy psfs appear to play in numerous imaging systems. The discussion in section 2 has surveyed *inferences* of stable laws that have been made from mtf measurements. Development of methods of analyzing imaging systems that can rigorously establish such laws, and predict the Lévy exponent β , would be a major advance.

Reconciling the results of section 2 with the behavior of large classes of images raises additional questions. Electronic imaging psfs $h(x, y)$ are found to have exponents $\beta > 0.5$ in most cases, so that $\log \hat{h}(\xi, 0) = -\alpha|\xi|^{2\beta}$ is a monotone decreasing concave function on $\xi > 0$. However, as illustrated in Figure 3, all images $g(x, y)$ used in this paper are such that global behavior in $-\log |\hat{g}^*(\xi, 0)|$ is generally monotone decreasing and *convex*. Another large class of images with this convexity property, the class **W**, was exhibited in [9]. When such images are APEX-fitted with a Lévy psf in the manner shown in Figure 5(B), a value of $\beta \leq 0.5$ is inevitably detected. An average value of $\beta = 0.23$ was found for the six images in Figures 4, 6, 11, 15, 16, and 17, and significantly lower values were found for the remaining three images in Figures 12, 13, and 14. A possible partial explanation for this discrepancy is provided by the Sydney experiment in Figure 1. There, the APEX method detected several useful psfs with values of β *smaller* than the value that was used to blur the image. The detected β -values in the above nine images may likewise underestimate the true imaging system β -values. An entirely different scenario may be that the

APEX method provides generic low exponent Lévy psfs capable of enhancing a wide variety of images, independently of the imaging physics that created them. Other generic enhancement techniques have been used for some time in image processing, [28, Chap. 10]. More recent approaches based on nonlinear diffusion equations are also intended as generic enhancement methods, [10]. However, such methods require large numbers of iterations and are not well suited for real-time processing of complex high resolution imagery.

Whatever may be the reasons behind it, the effectiveness of the APEX method on many types of images is undeniable, and the method is a useful addition to the image processing toolbox.

REFERENCES

- [1] O. BARNDORFF-NIELSEN, T. MIKOSCH AND S. RESNICK EDs., *Lévy Processes—Theory and Applications*, Birkhauser, Boston, 2001.
- [2] J. BERTOIN, *Lévy Processes*, Cambridge Tracts in Mathematics #121, 1998.
- [3] L. M. BIBERMAN AND S. NUDELMAN, *Photoelectronic Imaging Devices*, Plenum Press, New York, 1971.
- [4] P. BILER, G. KARCH, AND W. A. WOYCZYŃSKI, *Multifractal and Lévy conservation laws*, C. R. Acad. Sci. Paris, 330 (2000), pp. 343–348.
- [5] A. S. CARASSO, *Overcoming Hölder continuity in ill-posed continuation problems*, SIAM J. Numer. Anal., 31 (1994), pp. 1535–1557.
- [6] A. S. CARASSO, *Error bounds in nonsmooth image deblurring*, SIAM J. Math. Anal., 28 (1997), pp. 656–668.
- [7] A. S. CARASSO, *Linear and nonlinear image deblurring: a documented study*, SIAM J. Numer. Anal., 36 (1999), pp. 1659–1689.
- [8] A. S. CARASSO, *Logarithmic convexity and the ‘slow evolution’ constraint in ill-posed initial value problems*, SIAM J. Math. Anal., 30 (1999), pp. 479–496.
- [9] A. S. CARASSO, *Direct blind deconvolution*, SIAM J. Appl. Math., 61 (2001), pp. 1980–2007.
- [10] V. CASELLES, J. M. MOREL, G. SAPIRO, AND A. TANNENBAUM EDs., *Special Issue on Partial Differential Equations and Geometry-Driven Diffusion in Image Processing*, IEEE Transactions on Image Processing, 7, March 1998.
- [11] I. P. CSORBA ED., *Electron Image Tubes and Image Intensifiers*, SPIE Proceedings 1243 (1990).
- [12] I. P. CSORBA ED., *Electron Image Tubes and Image Intensifiers II*, SPIE Proceedings 1449 (1991).
- [13] W. FELLER, *An Introduction to Probability Theory and its Applications*, Vol. 2, Second ed., Wiley, New York, 1971.
- [14] R. E. FRANSEEN AND D. K. SCHRODER EDs., *Applications of Electronic Imaging Systems*, SPIE Proceedings 143 (1978).
- [15] R. E. HUFNAGEL AND N. R. STANLEY, *Modulation transfer function associated with image transmission through turbulent media*, J. Opt. Soc. Am., 54 (1964), pp. 52–61.
- [16] A. HECKERT AND J. J. FILLIBEN, *DATAPLOT Reference Manual*, available on World Wide Web at <http://www.itl.nist.gov/div898/software/dataplot/document.htm>
- [17] C. B. JOHNSON, *A method for characterizing electro-optical device modulation transfer functions*, Photographic Science and Engineering, 14 (1970), pp. 413–415.
- [18] C. B. JOHNSON, C. E. CATCHPOLE AND C. C. MATLE, *Microchannel plate inverter image intensifiers*, IEEE Transactions on Electron Devices, ED-18 (1971), pp. 1113–1116.
- [19] C. B. JOHNSON, *Classification of electron-optical device modulation transfer function*, Advances in Electronics and Electron Physics, Vol. 33B, (1972), pp. 579–584.
- [20] C. B. JOHNSON, *Circular aperture diffraction limited MTF: approximate expressions*, Applied Optics, 11 (1972), pp. 1875–1876.
- [21] C. B. JOHNSON, *MTFs: a simplified approach*, Electro-Optical Systems Design, 4, November 1972, pp. 22–26.
- [22] C. B. JOHNSON, *Point-spread functions, line-spread functions, and edge-response functions associated with mtf’s of the form $\exp[-(\omega/\omega_c)^n]$* , Applied Optics, 12 (1973), pp. 1031–1033.
- [23] C. B. JOHNSON, *A convenient form of graph paper for determination of electro-optical device modulation transfer function parameters*, IEEE Transactions on Electron Devices, ED-20

- (1973), pp. 80–81.
- [24] C. B. JOHNSON, *MTF parameters for all photographic films listed in Kodak pamphlet P-49*, Applied Optics, 15 (1976), p. 1130.
 - [25] C. B. JOHNSON, S. B. PATTON AND E. BENDER, *High-resolution microchannel plate image tube development*, SPIE Proceedings, 1449 (1991), pp. 2–12.
 - [26] C. B. JOHNSON AND B. N. LAPRADE (EDS.), *Electron Tubes and Image Intensifiers*, SPIE Proceedings 1655 (1992).
 - [27] R. KUSKE AND J. B. KELLER, *Rate of convergence to a stable law*, SIAM J. Appl. Math., 61 (2000), pp. 1308–1323.
 - [28] W. K. PRATT, *Digital Image Processing*, Second ed., Wiley, New York 1991.
 - [29] G. SAMORODNITSKY AND M. S. TAQQU, *Stable Non-Gaussian Random Processes: Stochastic Models with Infinite Variance*, Chapman and Hall, New York, 1991.
 - [30] M. F. SHLESINGER, G. M. ZASLAVSKY AND U. FRISCH (EDS.), *Lévy Flights and Related Topics in Physics*, Lecture Notes in Physics # 150, Springer-Verlag, New York, 1995.
 - [31] R. WEBER, *The ground-based electro-optical detection of deep-space satellites*, SPIE Proceedings, 143 (1978), pp. 59–69.
 - [32] C. S. WILLIAMS AND O. A. BECKLUND *Introduction to the Optical Transfer Function*, Wiley, New York, 1989.
 - [33] W. A. WOYCZYŃSKI, *Lévy processes in the physical sciences*, in *Lévy Processes—Theory and Applications*, O. Barndorff-Nielsen, T. Mikosch and S. Resnick (Eds.), Birkhauser, Boston 2001.

